Ten-year climatology of summertime diurnal rainfall rate over the conterminous U.S.

Toshihisa Matsui,[1,2] David Mocko,[3,4] Myong-In Lee,[5] Wei-Kuo Tao,[1] Max J. Suarez,[4] and Roger A. Pielke Sr.[6]

Received 28 May 2010; revised 4 June 2010; accepted 8 June 2010; published 10 July 2010.

[1] Diurnal cycles of summertime rainfall rates are examined over the conterminous United States, using radar-gauge assimilated hourly rainfall data. As in earlier studies, rainfall diurnal composites show a well-defined region of rainfall propagation over the Great Plains and an afternoon maximum area over the south and eastern portion of the United States. Using Hovmöller diagrams, zonal phase speeds of diurnal composite rainfall are estimated in three different small domains, and are evaluated with background meteorological conditions. These rainfall propagation speeds are better linked to the convective available potential energy than to the boundary-layer dryness. **Citation:** Matsui, T., D. Mocko, M.-I. Lee, W.-K. Tao, M. J. Suarez, and R. A. Pielke Sr. (2010), Ten-year climatology of summertime diurnal rainfall rate over the conterminous U.S., *Geophys. Res. Lett.*, *37*, L13807, doi:10.1029/2010GL044139.

1. Introduction

[2] Summertime rainfall over the conterminous U.S. is predominantly modulated by diurnal cycle. Pioneering work by *Wallace* [1975, hereafter WL75] depict geographical patterns of summertime diurnal rainfall (SDR) climatology through compiling decadal records of the 100s stations over United State. Recently, *Carbone and Tuttle* [2008, hereafter CT08] show more spatially complete picture of SDR climatology using operational radar echo. Both studies (and many others) agree that SDR are composed of two dominant modes: i) afternoon rainfall maxima due to mesoscale and local circulations over the south and east of the Mississippi and Ohio valleys, and ii) nocturnal rainfall maxima from propagating convective systems over the lee of Rockies.

[3] Thus, phase speed of the propagating convective rainfall should be of interest to understand dynamics that underlie the SDR structure over U.S. *Carbone et al.* [2002, hereafter CAR02] estimated zonal phase speed of propagating convective systems from the structure of Hovmöller diagram, and discussed possibility of two broad kinds of theories for the rainfall propagation mechanism: (i) boundary-layer disturbance due to cold air outflow (gust front) from convective downbursts [e.g., *Carbone et al.*, 1990] and many others), and (ii) convective gravity wave excitation due to latent heating at mid- to upper troposphere [e.g., *Moncrieff and Miller*, 1976].

[4] While CT08 provide the structure of SDR in terms of *rainfall frequency*, this study is motivated to provide quantitative (i.e., *rainfall rate*) maps of SDR over the conterminous U.S. using the novel radar-gauge assimilated rainfall. Then, in order to narrow the discussion by CAR02, we investigate the zonal phase speed of SDR in a different manner from CAR02. Therefore, results presented here can be compared to as well as compliment to CAR02, CT08 and WL75.

2. Rainfall Diurnal Cycle Maps and Hovmöller Diagrams

[5] This study compiled 1/8-degree hourly assimilated rainfall datasets from the North American Land Data Assimilation System (NLDAS) [*Cosgrove et al.*, 2003] for June-July-August (JJA) periods from 1998 to 2007, from NLDAS Phase II. This rainfall dataset covers the conterminous U.S. and is most predominantly derived by temporally disaggregating CPC (Climate Prediction Center) PRISM (Parameter-elevation Regressions on Independent Slopes Model)-adjusted daily rain gauge data using hourly weights from National Center for Environmental Prediction (NCEP) Stage II Doppler radar precipitation estimates. (Please see more details for data processing and validation in NLDAS website (http://ldas.gsfc.nasa.gov/.) Therefore, NLDAS rainfall data has the high temporal resolution, while it retains the magnitude of CPC daily rainfall data [*Higgins et al.*, 2000].

[6] By processing NLDAS rainfall data for ten years, each 1/8-degree grid has 22,080 samples that result in robust diurnal rainfall composites. Figure 1a shows a map of amplitude of the diurnal rainfall cycle (diurnal maximum minus minimum). In general, the deep south region features a large amplitude of the rainfall diurnal cycle, peaking in the middle of the Florida Peninsula (up to 1mm/hr), and becomes gradually weaker toward the interior of the continent. From the center of the domain to the southern Rocky Mountain, diurnal amplitudes appear to be relatively larger than surrounding regions. The western region features very weak amplitude of rainfall diurnal cycles attributable to dryness during summertime. These features are quite similar

[1]Laboratory for Atmospheres, NASA Goddard Space Flight Center, Greenbelt, Maryland, USA.
[2]GEST, University of Maryland Baltimore County, Baltimore, Maryland, USA.
[3]SAIC, Beltsville, Maryland, USA.
[4]GMAO, NASA Goddard Space Flight Center, Greenbelt, Maryland, USA.
[5]School of Urban and Environmental Engineering, UNIST, Ulsan, South Korea.
[6]Department of Atmospheric and Oceanic Sciences, CIRES, University of Colorado at Boulder, Boulder, Colorado, USA.

0094-8276/10/2010GL044139

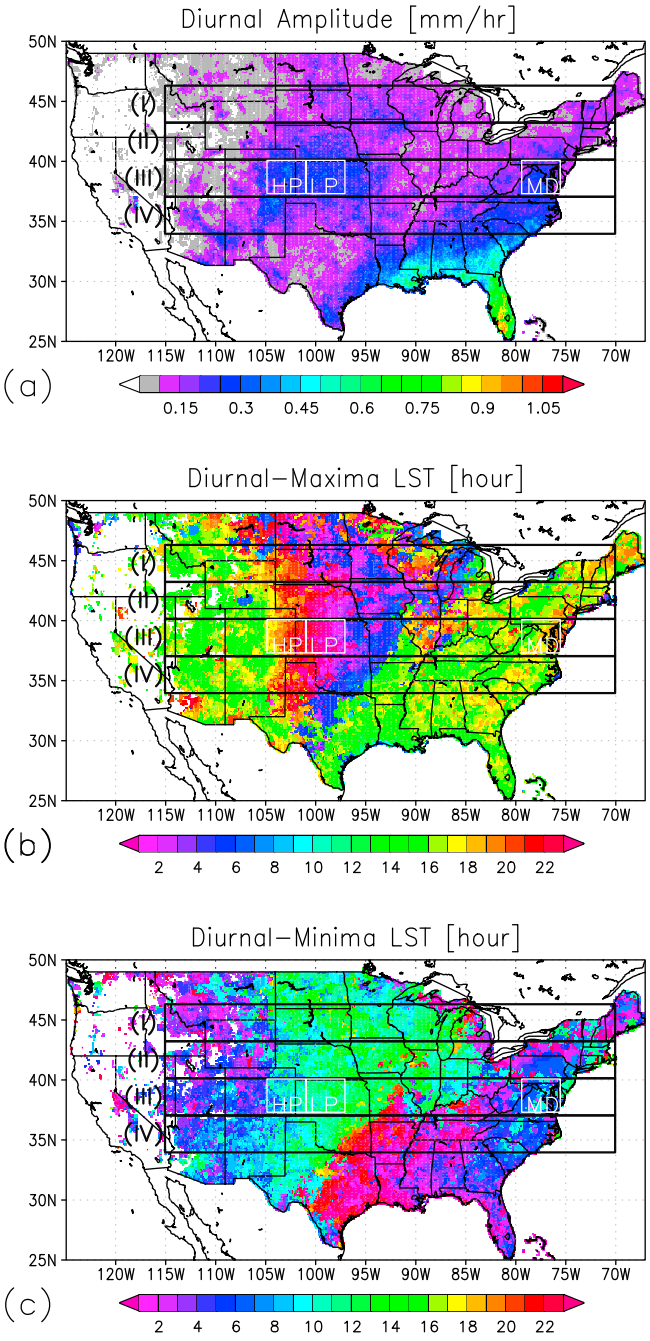

Figure 1. Ten-year JJA climatology of (a) diurnal amplitude (diurnal maximum minus minimum) of rainfall rate, (b) local solar time (LST) of diurnal maxima, and (c) LST of diurnal minima.

to the corresponding map from an independent rainfall data [*Kikuchi and Wang*, 2008].

[7] Figures 1b and 1c show maps of the maximum and minimum rainfall hour indicated in local solar time (LST), respectively. (Pixels with very small diurnal amplitude (less than 0.1mm/hr in Figure 1a) are masked out in Figures 1b and 1c.) Over southern and northeast regions, the diurnal maxima typically range from local noon to the late afternoon. Local noon maxima are particularly well defined over the Appalachian Mountains and coastal regions, while late-afternoon maxima appear between these two regions. In the same south and northeast regions, rainfall minimum LST ranges from 0000LST to 1000LST towards the east.

[8] Figure 1b depicts a triangle zone with a gradual change of diurnal-maxima LST over the Great Plains. The diurnal-maxima LST changes approximately from local early afternoon to early morning, as it moves eastward, due to long-lasting (300 km ~ 1000 km), eastward-propagating convective systems discussed in CAR02 and WL75. In this area, the diurnal-minima LST also vary from local midnight to late afternoon (Figure 1c).

[9] Following CAR02 and CT08, we have constructed Hovmöller diagrams (Figure 2), which describe the variability of rainfall rate as a function of longitude (bin size: 0.125°) versus time (bin size: 1hr) using universal time (UT). We have set up four areas (I: 43°N ~ 46°N; II: 40°N ~ 43°N; III: 37°N ~ 40°N; and IV: 34°N ~ 37°N) from north to south extending in longitude from 115°W to 70°W (Figures 1b or 1c). From 115°W to 105°W, the rainfall rate peaks at 1500LST driven by mountain valley circulations. From 105°W to 95°W, as shown in Figure 1b, the diurnal-maxima time shifts from afternoon, to night, and to early morning, from west to east. Among all areas, Area III has the most robust rainfall pattern (rainfall rate: ~0.28mm/hr), in which the Great Plains low-level jet supplies moisture that could sustain propagating rainfall systems [*Higgins et al.*, 1997].

[10] From 95°W to 85°W, diurnal rainfall peaks switch dominant signals from early morning to late afternoon. This transition explains the sudden changes of maxima and minima LST extending from southwest to northeast regions in Figures 1b and 1c. Because of the presence of multi-mode diurnal rainfall, amplitudes appear to be relative small in Figure 1a. Area I and II tend to have multiple modes, and the structure of the rainfall diurnal cycle indicates the presence of propagating system elsewhere in this zone (see solid line in Figure 2). From 85°W to 70°W, the mesoscale and local circulation contributes to the dominant afternoon rainfall signal, with the presence of relatively weak nocturnal modes. The afternoon signals become especially predominant in Area IV. Area III shows clear rainfall diurnal signals from propagating rainfall system from the Appalachian Mountains.

[11] Over all, these patterns of SDR climatology agree with those in CT08 using radar echo frequency (i.e., rainfall count). However, simply because our study uses *rainfall rate*, our SDR climatology are more weighted toward heavy organized rainfall systems, such as Mesoscale Convective Complexes (please see details in the auxiliary material).[1]

3. Rainfall Phase Speed Characteristics

[12] Propagating rainfall systems characterize the patterns of SDR over large areas of the conterminous U.S. Thus, assessment of zonal phase speed becomes an important topic. While CAR02 estimated individual MCC phase speed from Hovmöller diagrams over the large U.S. domains, our analysis focuses on three small sub-domains of Area III in Figure 2: High Plain (HP: 105°W ~ 102°W), Low Plain (LP: 101°W ~ 98°W), and Maryland (MD: 79°W ~ 76°W)[1].

[1]Auxiliary materials are available in the HTML. doi:10.1029/2010GL044139.

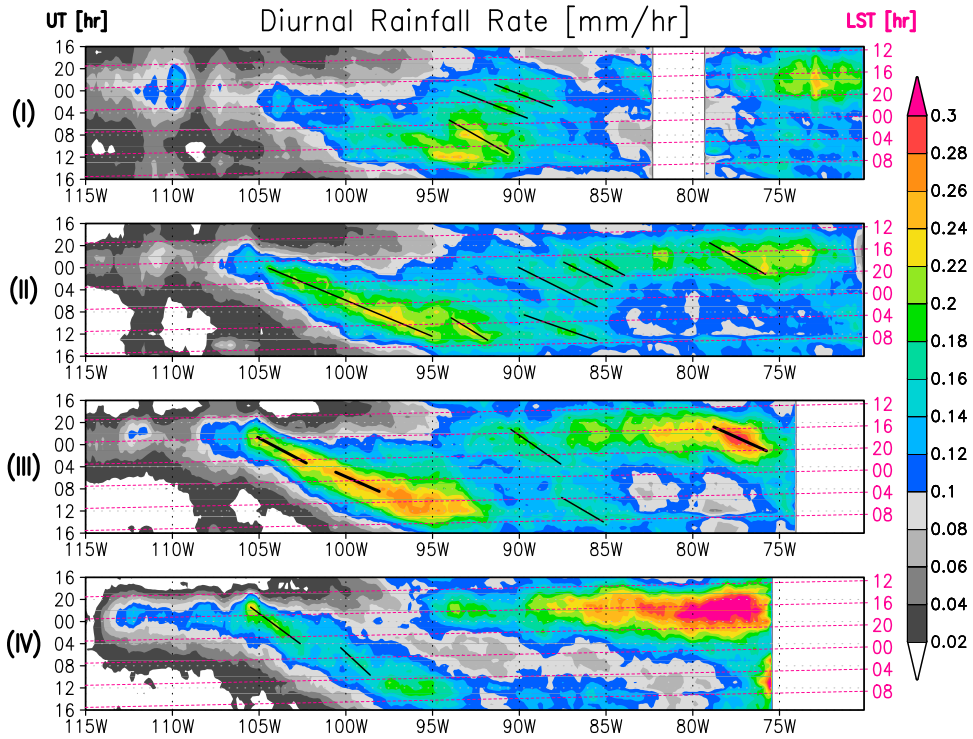

Figure 2. Hovmöller diagrams of rainfall rate [mm/hr] in Areas I (43°N ~ 46°N), II (40°N ~ 43°N), III (37°N ~ 40°N), and IV (34°N ~ 37°N). Solid lines suggest presence of rainfall propagation.

Each of these domains represents robust signals of SDR with different zonal phase speed of propagating rainfall systems (Figure 2). These three regions have different background meteorological and geographical conditions. Therefore, by applying different propagation mechanisms to three regions, we could have a better chance to identify the weakness and the strength of the proposed theory.

[13] The zonal phase speed of propagation was estimated from linear regression method to the diurnal-maxima time (each 0.125° longitude bin). Estimated zonal phase speeds of the diurnal composite rainfall (*Vs*) are 15.7m/s, 19.2m/s, and 20.7m/s in the HP, LP, and MD domains, respectively, which are comparable to CAR02. HP has the slowest *Vs* starting at 2329UT on the Rocky Mountain, while MD has the fastest *Vs* starting at 2100UT. In the HP and MD domains, rainfall systems are typically initiated by mountain valley circulation around local 3pm to 4pm [*Tripoli and Cotton*, 1989a]. LP domain shows propagating nocturnal rainfall, starting at 0434UT and ending at 0802UT. Although there is no clear definition of uncertainty in estimated zonal phase speed, the spread of precipitation rate in Hovmöller diagram could suggest uncertainty level.

[14] Next, we have investigated wind and thermodynamic profiles from the Modern Era Retrospective-Analysis for Research and Analysis (MERRA) [*Bosilovich et al.*, 2006]. MERRA parameters are sampled through the identical sampling method in the NLDAS ten-year JJA Hovmöller diagrams, and are averaged along regressed phase lines and over domains. In this way, averaged MERRA parameters characterize the mean state of the background meteorology of *Vs* (Figure 4).

[15] Figure 4a shows zonal wind profiles and *Vs*. 200 mb-level zonal wind speeds in HP and MD appear to be very close to the corresponding *Vs*, while the 200 mb wind is 5 m/s less than *Vs* in the LP domain. Instead of choosing an arbitrary single-level zonal wind in CAR02, we estimate the steering wind with respect to profiles of buoyant force (F_b),

$$F_b = \frac{Tv_{parcel} - Tv_{env}}{Tv_{env}} g, \tag{1}$$

where Tv_{parcel} and Tv_{env} are virtual atmospheric temperatures of an adiabatically lifted parcel from the lowest the reanalysis level and of the surrounding environment, respectively; g is the acceleration of gravity. We have averaged *Fb* (upward buoyant force only) during the same time period to estimate climatologically expected buoyant profiles in three domains (Figure 4b).

[16] Variability of *Fb* essentially represents mean profiles of convection intensity, which are unique in the three different regions. *Fb* peaks at the 500mb level in HP and LP domains, while it peaks at the 650 mb level in the MD domain (Figure 4b). Then, we estimate steering wind (U_s) by normalizing zonal wind profile by F_b:

$$U_s = \frac{\int u \cdot F_b \, dp}{\int F_b \, dp}. \tag{2}$$

Estimated U_s of HP, LP, and MD domains are, in that order, 6.5 m/s, 7.3 m/s, and 8.4 m/s, which correspond to the 500 mb-level, 550 mb-level, and 600 mb-level zonal wind speeds, which appears to be comparable with CAR02. Thus, rainfall propagation speeds (*Vp*) are estimated from the difference between the zonal phase speed (V_s) of the rainfall and the steering wind speed (U_s) ($Vp = V_s - U_s = 9.2$ m/s in HP, 11.9 m/s in LP, and 12.2 m/s in MD) following CAR02.

[17] A gust front is the cold outflow from thunderstorms, driven partially by rainfall drag and mainly by downdraft of

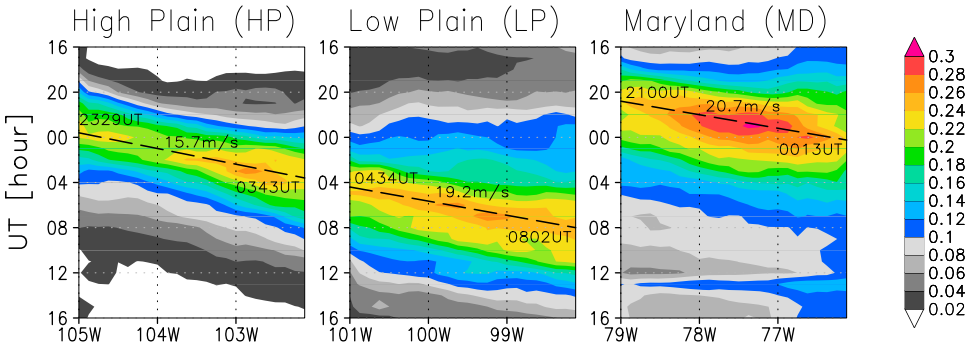

Figure 3. Hovmöller diagrams of rainfall rate [mm/hr] for HP, LP, and MD domains (37°N ~ 40°N). Intercept (UT) at the western and eastern edge of domains are starting and ending UT, respectively. Estimated zonal phase speeds of rainfall are also shown.

cool air mass due to evaporation of falling raindrops. The gust front proceeds ahead of the main core of the thunderstorm, and induces additional convection by disturbing the conditionally unstable atmosphere [*Carbone et al.*, 1990]. A common semi-empirical formula of the gust front speed (i.e., density current) following *Seitter* [1986] is:

$$V_d = k^* \cdot \left[gH \cdot \frac{Tv_{den} - Tv_{env}}{Tv_{env}} \right]^{0.5}, \quad (3)$$

where k^* is internal Froude number, ranging from 0.72 to 1.08 [*Wakimoto*, 1982]; g is the acceleration of gravity; H is head height of density current which can be up to about 4000 m [*Wakimoto*, 1982]; and Tv_{den} and Tv_{env} are virtual temperature of the gust front and surrounding environment, respectively. To apply MERRA data, some assumptions were made: (a) Tv_{env} is the surrounding virtual temperature at the above-ground height of H; (b) Tv_{den} is the dewpoint virtual temperature at the above-ground height of H, meaning that surface air mass is cooled at maximum rate by rainfall evaporation. Thus the previous equation is arranged to

$$V_d = k^* \cdot \left[gH \cdot \left(\frac{\Delta Tv_{dew}}{Tv} \right)_H \right]^{0.5}. \quad (4)$$

We apply MERRA data to the above equation, and estimate Vd for the HP, LP, and MD domains as a function of H (250 m ~ 2000 m) with three different k^* (0.72, 0.9, and 1.08), because H and k^* remain uncertain (Figure 4c).

[18] Figure 4c shows the variation of Vd with estimated Vp for HP, LP, and MD domains. It is obvious that the Vd can agree with Vp for some combinations of H and k^*. Considering fixed H to be 1000m and k^* to be 0.9, Vd becomes about 16 m/s in HP, 14 m/s in LP, and 12 m/s in MD domains. This is because boundary-layer dewpoint depression (thus negative buoyant force in equation (3)) becomes larger from MD, to LP, and to HP. The point here is that drier (moister) boundary-layer air in HP (MD) always creates the fastest (slowest) Vd, which appears to contradict the order of estimated Vp (i.e., MD > LP > HP). Alternatively, one may argue that geographical variability of the mean gust front head height (H) could explain such contradicts. However, the gust front is a dissipative and dispersive current; H and Vd vary depending on the distance away from the downburst core [*Wakimoto*, 1982]. It should be also noted that moisture content above the boundary layer is not accounted in this analysis.

[19] Another theory of rainfall propagation is internal gravity waves in the free troposphere due to ensemble of latent heating and evaporative cooling. For example, *Moncrieff and Miller* [1976] developed a three-dimensional analytical model, and explained that rainfall propagation speed can be simply explained by square root of convective available potential energy (CAPE): i.e.,

$$V_d \approx c \cdot (CAPE)^{0.5}, \quad (5)$$

where c is 0.32 under some assumptions in the case of tropical squall line [*Moncrieff and Miller*, 1976]. We adapt MERRA to compute and integrate CAPE (positive buoyant force only) during the identical analysis period; i.e., CAPE is sampled in space and time along the rainfall phase line in Figure 3. Note that we CAPE is integrated one hour before the rainfall diurnal-maxima time as well as lagged ±1hr. Figure 4d shows the relationship between Vp and $(CAPE)^{0.5}$.

[20] Although it is only three points, it has a positive correlation that explains Vp order between HP and LP, although it cannot explain the difference between LP and MD. The slope (c) is about 0.53, which is substantially larger than the values used (c = 0.32) by *Moncrieff and Miller* [1976]. This discrepancy is not surprising, because our study focuses on observations in the mid-latitude organized rainfall, whereas *Moncrieff and Miller* [1976] focused on tropical squall lines and they developed an analytical solution under several assumptions.

4. Remarks

[21] We have applied simple linear theories to explain zonal phase speed of rainfall in three different geographic domains. Results *qualitatively* indicate that the latent heat release (as a function of CAPE [*Moncrieff and Miller*, 1976]) together with background steering wind speed are a more robust theory that explains the unique rainfall propagation speeds in the three different geographic domains, rather than the effect of boundary-layer gust front disturbance (as a function of boundary-layer dryness).

[22] However, results could be quantitatively inconclusive due to i) the inherent assumptions in the linear theories, ii) the uncertainties of MERRA (and possibly all other global reanalysis) in near-surface temperature and humidity, and

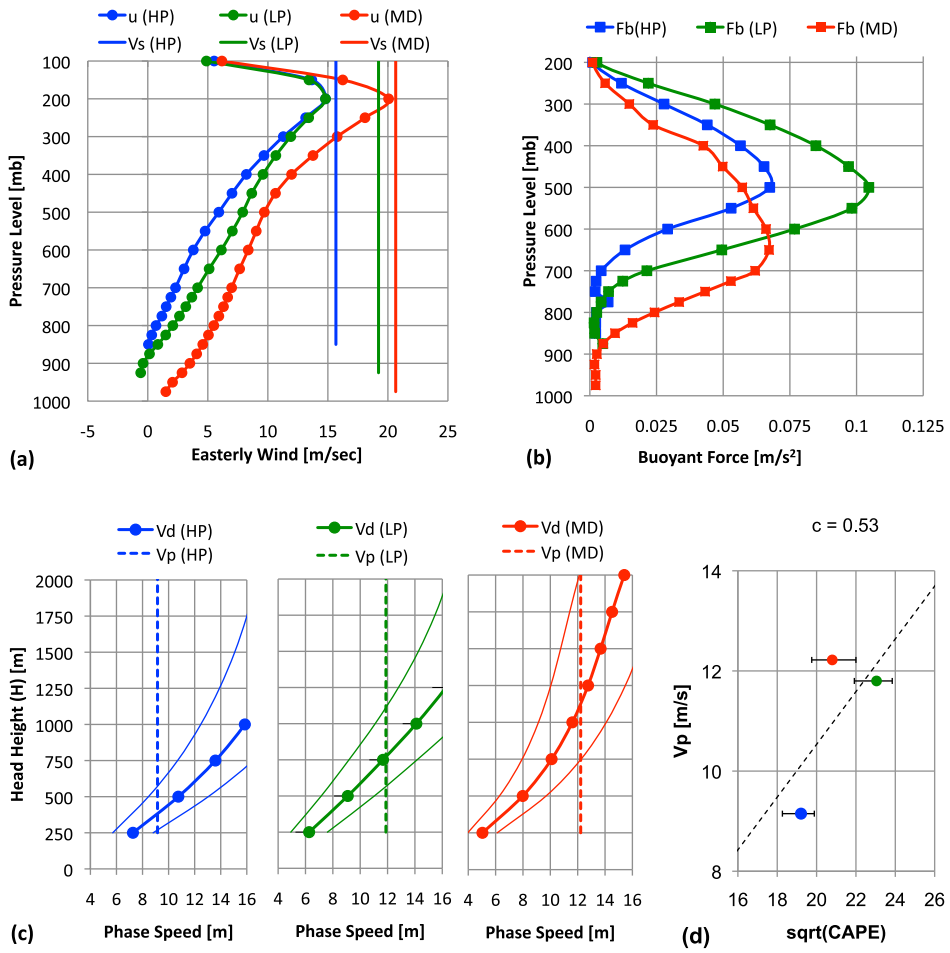

Figure 4. (a) Zonal phase speed of rainfall streak (*Vs*: vertical solid line) versus profiles of zonal wind speed (*u*: solid line with circle) from MERRA, (b) profiles of buoyant force (*Fb*) from MERRA, (c) rainfall propagation speed ($Vp = Vs - Us$: vertical dot line) versus estimated gust front speed (*Vd*: solid line $k^* = 0.72$ and 1.08, solid line with circle $k^* = 0.9$) from MERRA, and (d) rainfall propagation speed (*Vp*) versus square root of CAPE. Error bars represent plus- and minus-1hr lagged CAPE values. Dot line represents regressed line with zero intercept (slope: $c = 0.53$).

iii) uncertainties in estimated zonal phase speed of SDR climatology. Nevertheless, completion of discussion in rainfall propagation theory is beyond the scope in this short manuscript. Propagation of convective precipitation system can be better explained by complex interactions between background mean flow speed and shear as well as mesoscale dynamics associated latent heat release, evaporating cooling, and radiative cooling [*Tripoli and Cotton*, 1989b]. None of the current global weather or climate models has capability to resolve SDR over the U.S. [*Lee et al.*, 2007]. Thus, we need large-scale, long-term, and meso-γ-scale model simulations to investigate rainfall propagation mechanisms for future study.

[23] Nevertheless, these results will be a useful benchmark of SDR for various analysis and validation for weather and climate models. We present this new analysis as a compliment to WL75, CAR02, and CT08. Complete discussion and citations of SDR are also found in those manuscripts. The data used in this manuscript are archived and distributed by the Goddard Earth Sciences (GES) Data and Information Services Center (DISC) (http://disc.sci.gsfc.nasa.gov/).

[24] **Acknowledgments.** This work was supported by the NASA Modeling Analysis and Prediction project. The authors are grateful to Dr. D. Cosidine at NASA HQ. The NLDAS project is a collaboration project among several groups and funded with support from NOAA's Climate Prediction Program for the Americas (CPPA). We thank Brian Cosgrove and Charles Alonge for leading the development of the NLDAS Phase II rainfall product.

References

Bosilovich, M., S. D. Schubert, G. Kim, R. Gelaro, M. Rienecker, M. Suarez, and R. Todling (2006), NASA's Modern Era Retrospective-analysis for Research and Applications (MERRA), *U.S. CLIVAR Var.*, *4*, 5–8.

Carbone, R. E., and J. D. Tuttle (2008), Rainfall occurrence in the United States warm season: The diurnal cycle, *J. Clim.*, *21*, 4132–4146, doi:10.1175/2008JCLI2275.1.

Carbone, R. E., J. W. Conway, N. A. Crook, and M. W. Moncrieff (1990), The generation and propagation of a nocturnal squall line. Part I: Observations and implications for mesoscale predictability, *Mon. Weather Rev.*, *118*, 26–49, doi:10.1175/1520-0493(1990)118<0026:TGAPOA>2.0.CO;2.

Carbone, R. E., J. D. Tuttle, D. A. Ahijevych, and S. B. Trier (2002), Inferences of predictability associated with warm season precipitation episodes, *J. Atmos. Sci.*, *59*, 2033–2056, doi:10.1175/1520-0469(2002)059<2033:IOPAWW>2.0.CO;2.

Cosgrove, B. A., et al. (2003), Real-time and retrospective forcing in the North American Land Data Assimilation System (NLDAS) project, *J. Geophys. Res.*, *108*(D22), 8842, doi:10.1029/2002JD003118.

Higgins, R. W., Y. Yao, and X. L. Wang (1997), Influence of the North American monsoon system on the US summer precipitation regime, *J. Clim.*, *10*, 2600–2622, doi:10.1175/1520-0442(1997)010<2600:IOTNAM>2.0.CO;2.

Higgins, R.W., W. Shi, E. Yarosh, and R. Joyce (2000), Improved United States precipitation quality control system and analysis, *NCEP Clim. Predict. Cent. ATLAS 7*, 40 pp., Camp Springs, Md.

Kikuchi, K., and B. Wang (2008), Diurnal precipitation regimes in the global tropics, *J. Clim.*, *21*, 2680–2696, doi:10.1175/2007JCLI2051.1.

Lee, M. I., S. D. Schubert, M. J. Suarez, I. M. Held, N. C. Lau, J. J. Ploshay, A. Kumar, H. K. Kim, and J. K. E. Schemm (2007), An analysis of the warm-season diurnal cycle over the continental United States and northern Mexico in general circulation models, *J. Hydrometeorol.*, *8*, 344–366, doi:10.1175/JHM581.1.

Moncrieff, M. W., and M. J. Miller (1976), The dynamics and simulation of tropical cumulonimbus and squall lines, *Q. J. R. Meteorol. Soc.*, *102*, 373–394, doi:10.1002/qj.49710243208.

Seitter, K. L. (1986), A numerical study of atmospheric density current motion including the effects of condensation, *J. Atmos. Sci.*, *43*, 3068–3076, doi:10.1175/1520-0469(1986)043<3068:ANSOAD>2.0.CO;2.

Tripoli, G. J., and W. R. Cotton (1989a), Numerical study of an observed orogenic mesoscale convective system. Part 1: Simulated genesis and comparison with observations, *Mon. Weather Rev.*, *117*, 273–304, doi:10.1175/1520-0493(1989)117<0273:NSOAOO>2.0.CO;2.

Tripoli, G. J., and W. R. Cotton (1989b), Numerical study of an observed orogenic mesoscale convective system. Part 2: Analysis of governing dynamics, *Mon. Weather Rev.*, *117*, 305–328, doi:10.1175/1520-0493(1989)117<0305:NSOAOO>2.0.CO;2.

Wakimoto, R. M. (1982), The life cycle of thunderstorm gust fronts as viewed with Doppler radar and rawinsonde data, *Mon. Weather Rev.*, *110*, 1060–1082, doi:10.1175/1520-0493(1982)110<1060:TLCOTG>2.0.CO;2.

Wallace, J. M. (1975), Diurnal variations in precipitation and thunderstorm frequency over the conterminous United States, *Mon. Weather Rev.*, *103*, 406–419, doi:10.1175/1520-0493(1975)103<0406:DVIPAT>2.0.CO;2.

M.-I. Lee, School of Urban and Environmental Engineering, UNIST, Banyeon-ri 100, Eonyang-eup, Ulju-gun, Ulsan 689-798, South Korea.

T. Matsui and W.-K. Tao, Laboratory for Atmospheres, NASA Goddard Space Flight Center, Code 613.1, Greenbelt, MD 20771, USA.

D. Mocko, SAIC, 4600 Powder Mill Rd., Ste. 400, Beltsville, MD 20705, USA.

R. A. Pielke Sr., Department of Atmospheric and Oceanic Sciences, CIRES, University of Colorado at Boulder, 216 UCB, Boulder, CO 80309-2016, USA.

M. J. Suarez, GMAO, NASA Goddard Space Flight Center, Code 610.1, Greenbelt, MD 20771, USA.